

# Kratos-polrad: Novel GPU system for Monte-Carlo simulations with consistent polarization calculations

HAIFENG YANG (杨海峰) <sup>1, 2, \*</sup> AND LILE WANG (王力乐) <sup>3, 4</sup>

<sup>1</sup>*Institute for Astronomy, School of Physics, Zhejiang University, 886 Yuhangtang Road, Hangzhou 310027, China*

<sup>2</sup>*Center for Cosmology and Computational Astrophysics, Institute for Advanced Study in Physics, Zhejiang University, Hangzhou 310027, China*

<sup>3</sup>*The Kavli Institute for Astronomy and Astrophysics, Peking University, Beijing 100871, China*

<sup>4</sup>*Department of Astronomy, School of Physics, Peking University, Beijing 100871, China*

## ABSTRACT

Polarized radiation serves as a vital diagnostic tool in astrophysics, providing unique insights into magnetic field geometries, scattering processes, and three-dimensional structures in diverse astrophysical scenarios. To address these applications, we present Kratos-polrad, a novel GPU-accelerated Monte Carlo Radiative Transfer code built upon the heterogeneous computing framework of Kratos, designed for self-consistent and efficient polarization calculations. It utilizes comprehensive treatment of Stokes parameters throughout photon propagation, featuring transforms the grain-lab frame transforms using quaternion algebra and consistent non-linear polarization extinction in cells, which are useful in modeling radiative transfer processes with scatterings by aligned dust grains. The code implements two-step polarimetry imaging that decouples Monte Carlo sampling of scattering physics from imaging geometry, enabling efficient synthesis maximizing the utilization of photon packets. Extensive validation against analytical solutions and established codes demonstrates accurate treatment of diverse polarization phenomena, including self-scattering polarization, dichroic extinction in aligned dust grains, and complex polarization patterns in twisted magnetic field configurations. By leveraging massive GPU parallelism, optimized memory access patterns, and analytical approaches for optically thick cells, Kratos-polrad achieves performance improvements of  $\sim 10^2$  times compared to CPU-based methods, enabling previously prohibitive studies in polarimetric astrophysics.

**Keywords:** Interstellar dust extinction(837), Protoplanetary disks(1300), Radiative transfer simulations(1967), Computational methods(1965), GPU computing(1969)

## 1. INTRODUCTION

Polarized radiation serves as a powerful diagnostic tool across virtually all domains of astrophysics, from the scattering atmospheres of exoplanets, (S. Seager et al. 2000; T. Stolker et al. 2017), circumstellar disks (e.g. M. Benisty et al. 2023; I. W. Stephens et al. 2023), AGB outflows (S. Ramstedt et al. 2011), through the complex environments of active galactic nuclei (J. F. Kartje 1995; F. Marin et al. 2015) and supernova remnants (M. Bocchio et al. 2016). The polarization state of photons encodes unique information about magnetic field geometries, scattering optical depths, and the three-

dimensional structure of emitting regions that cannot be accessed through intensity measurements alone. As observational facilities with polarimetric capabilities continue to advance, including SPHERE/ZIMPOL (H. M. Schmid et al. 2018), and future instruments like the Origins Space Telescope (A. Cooray et al. 2019), the demand for sophisticated theoretical models capable of predicting detailed polarization signatures has never been more urgent.

The fundamental challenge in modeling polarized radiation lies in solving the vector radiative transfer equation, which tracks not just photon intensities but also the full Stokes parameters ( $I, Q, U, V$ ) that characterize the polarization state (S. Chandrasekhar 1960). For astrophysical environments characterized by multiple scattering events and complex geometries, Monte Carlo methods have emerged as the approach of choice (B. A.

Corresponding author: Lile Wang  
lilew@pku.edu.cn

\* ZJU Tang Scholar

Whitney et al. 2013). These methods stochastically sample photon paths and scattering events, naturally handling three-dimensional geometries, arbitrary optical depth distributions, and multiple scattering without the limitations of diffusion approximations. However, traditional Monte Carlo radiative transfer (MCRT) codes face severe computational limitations when applied to polarimetric problems. Each scattering event modifies the Stokes vector according to Mueller matrices that depend on scattering angles and local properties, requiring extensive calculations of directional sampling and polarization state tracking. Furthermore, synthesizing observables such as images and polarization maps demands Monte Carlo sampling of the entire radiation field, often requiring  $10^8$ – $10^{10}$  photon packets for convergence in complex geometries (e.g. P. Camps & M. Baes 2015).

The computational demands of polarized MCRT have historically restricted its application to simplified geometries or limited parameter explorations. While several highly optimized codes exist—including RADMC-3D (C. P. Dullemond et al. 2012), MCFOST (C. Pinte et al. 2006), POLARIS (S. Reissl et al. 2016), SKIRT (P. Camps & M. Baes 2015, 2020), and Hyperion (T. P. Robitaille 2011)—most rely on CPU-based architectures that struggle to meet the computational requirements of modern polarimetric studies. The emergence of heterogeneous computing architectures, particularly Graphics Processing Units (GPUs), offers a transformative solution. Recent efforts to port radiative transfer to GPUs have demonstrated remarkable speedups (e.g. M. Malik et al. 2017; C. Byrohl & D. Nelson 2025). However, these GPU implementations have largely focused on scalar intensity calculations, with polarization support remaining limited or completely absent.

In diverse astrophysical environments, from molecular clouds to protoplanetary disks, interstellar dust grains frequently exhibit non-random alignment relative to local physical fields (J. S. Hall 1949; W. A. Hiltner 1949). The prevailing alignment mechanism in most scenarios involves relaxation that orients grains with their short axes parallel to magnetic field lines (B.-G. Andersson et al. 2015, and references therein). This magnetic alignment paradigm provides a powerful tool for studying cosmic magnetic fields through their imprint on polarized radiation. Notable exceptions exist, particularly at small scales such as the dense mid-planes of protoplanetary disks where large grains may experience alignment through radiative torques (A. Lazarian & T. Hoang 2007; R. Tazaki et al. 2017) or dust-gas differential motions (H. Yang et al. 2019; Z.-Y. D. Lin et al. 2024a) rather than magnetic fields. Understanding these competing alignment mechanisms is crucial for interpreting

polarization observations across different astrophysical contexts.

Scattering by aligned dust grains produces distinctive polarization signatures that can potentially serve as powerful diagnostics of embedded magnetic field geometries. At near-infrared wavelengths, magnetically aligned grains produce deviation from oft-adopted azimuthal orientations on order of  $10^\circ$ , or even perpendicular direction in extreme cases (large toroidal magnetic field component with high inclination angle) (H. Yang & Z.-Y. Li 2022). At millimeter and submillimeter wavelengths, accessible with facilities like ALMA (Atacama Large Millimeter/submillimeter Array), the light source becomes dust thermal emission, instead of stellar illumination. At these longer wavelengths, both emission from aligned grains and scattering contributions can produce significant polarization, with their relative importance depending on grain properties, optical depth, and source geometry (H. Yang et al. 2016b; Z.-Y. D. Lin et al. 2022, 2024b). Understanding this transition is essential for correctly interpreting polarization maps that probe the dust grain properties, as well as magnetic fields and/or gas dynamic environments, where planets form.

Despite the astrophysical importance of polarized scattering by aligned grains, the radiative transfer community currently lacks comprehensive tools capable of self-consistently modeling these effects. In this paper, we present Kratos-polrad<sup>1</sup>, a polarization-informed Monte Carlo radiative transfer module built upon the Kratos framework. The Kratos Framework (L. Wang 2025a) represents a GPU-optimized astrophysical simulation system designed for heterogeneous computing architectures across CUDA, HIP, and CPU platforms. The modular architecture separates mesh management from physical solvers, enabling straightforward extension to the desired radiative transfer polarimetry calculations desired. Our implementation features full treatment of Stokes parameters throughout photon propagation and scattering, and efficient imaging synthesis using scattering source functions.

This paper presents the methodology, verification, and performance characteristics of Kratos-polrad. § 2 details our Monte Carlo algorithm for polarized transport, the scattering source function formalism, and GPU-specific optimizations. § 3 validates the code through standard radiative transfer benchmarks against (semi-)analytic solutions for plane-parallel polarization, together with demonstrations of the computational advantages with

<sup>1</sup> [https://github.com/wll745881210/kratos\\_polrad.git](https://github.com/wll745881210/kratos_polrad.git)

GPU algorithms. We conclude in § 4 by outlining future generalizations and astrophysical applications.

## 2. METHODS

Kratos-polrad employs a GPU-accelerated Monte Carlo framework built upon the Kratos simulation system (L. Wang 2025a), utilizing the grid-based ray-tracing method described in L. Wang (2025b). A composite mesh grid, optionally enhanced with static mesh refinement, stores the physical state variables. Photon packets propagate through this grid, undergoing emission, absorption along their path, and scattering events that redirect their trajectories. However, polarization-aware calculations require additional treatment: the Stokes parameters carried by each photon packet must be transformed via Mueller matrices at every scattering interaction, and the accumulated polarization state must be tracked throughout the photon’s lifecycle to enable synthesis of polarized observables.

### 2.1. Quaternion-based coordinate transformations for polarized radiative transfer

The accurate treatment of polarized radiative transfer requires precise coordinate transformations at each scattering event, as both the photon propagation direction and polarization state must be consistently rotated between the global simulation frame and the local frame defined by the scattering body orientation. Traditional approaches using Euler angles or rotation matrices suffer from numerical instabilities (e.g., gimbal lock) and possible convention confusions. To overcome these limitations, we employ Hamilton’s quaternions, which provide a compact representation of rotations that enables stable, efficient composition of successive transformations directly in GPU registers. A quaternion  $\mathbf{q} = q_0 + q_1\mathbf{i} + q_2\mathbf{j} + q_3\mathbf{k}$  extends complex numbers into four dimensions, where the basis elements satisfy the fundamental relations:

$$\mathbf{i}^2 = \mathbf{j}^2 = \mathbf{k}^2 = \mathbf{ijk} = -1. \quad (1)$$

This algebraic structure provides a natural representation for three-dimensional rotations without the singularities inherent in other parameterizations.

In polarized radiative transfer through aligned dust grains, the local scattering frame (the “Grain Frame”) is determined by the symmetry axis of the dust particles. For this work, we assume perfect alignment with the local magnetic field direction, characterized by position angles  $(\theta_B, \phi_B)$  in global spherical coordinates. The rotation from the global frame to the Grain Frame

is represented by the quaternion:

$$\mathbf{q}_B = \begin{cases} q_{B,0} = \cos(\phi_B/2) \cos(\theta_B/2) \\ q_{B,1} = -\sin(\phi_B/2) \sin(\theta_B/2) \\ q_{B,2} = \cos(\phi_B/2) \sin(\theta_B/2) \\ q_{B,3} = \sin(\phi_B/2) \cos(\theta_B/2) \end{cases}, \quad (2)$$

which follows the convention established in the `quaternion` Python module (M. Boyle et al. 2025). This specific form ensures proper handling of the double coverage of the rotation group by quaternions.

For a photon propagating along direction  $\hat{n}$  in the global frame, its representation in the Grain Frame  $\hat{n}_{GF}$  is obtained through the quaternion conjugation:

$$(0, \vec{n}_{GF}) = \mathbf{q}_B^* \cdot (0, \vec{n}) \cdot \mathbf{q}_B, \quad (3)$$

where  $(0, \vec{n})$  denotes a pure quaternion (zero scalar component) constructed from the vector components, and  $\mathbf{q}_B^*$  represents the quaternion conjugate. This operation efficiently rotates the propagation direction into the local grain-aligned frame, which determines the incident direction for scattering calculations.

The transformation of polarization states requires careful treatment of the reference direction conventions. We adopt a convention where for light propagating along direction  $(\theta, \phi)$ , the Stokes parameters are defined relative to the spherical coordinate basis vectors:

$$\hat{\theta} = (\cos \theta \cos \phi, \cos \theta \sin \phi, -\sin \theta), \quad (4)$$

$$\hat{\phi} = (-\sin \phi, \cos \phi, 0). \quad (5)$$

In this convention, positive Stokes  $Q$  corresponds to linear polarization along the  $\hat{\theta}$  direction, while negative  $Q$  indicates polarization along  $\hat{\phi}$ . When rotating to the Grain Frame, the reference direction  $\hat{\phi}$  from the global frame transforms to  $\hat{\phi}_{GF}$  in the Grain Frame. However, this differs from the natural  $\hat{\phi}'$  direction defined by the rotated propagation vector  $\hat{n}_{GF}$ . The angle  $\eta$  between these two directions is computed via the cross product:

$$\sin \eta = |\hat{\phi}_{GF} \times \hat{\phi}'|, \quad \cos \eta = \hat{\phi}_{GF} \cdot \hat{\phi}'. \quad (6)$$

This angle  $\eta$  then rotates the linear polarization components according to:

$$\begin{pmatrix} Q' \\ U' \end{pmatrix} = \begin{pmatrix} \cos 2\eta & \sin 2\eta \\ -\sin 2\eta & \cos 2\eta \end{pmatrix} \begin{pmatrix} Q \\ U \end{pmatrix}, \quad (7)$$

while Stokes  $I$  and  $V$  remain invariant under this reference frame rotation.

## 2.2. Radiative transfer equations

The propagation of polarized radiation through astrophysical media is governed by the vector radiative transfer equation, which extends the scalar form to track the full Stokes vector  $\mathcal{I} \equiv (I, Q, U, V)^T$ . For each frequency bin (suppressed for notational clarity), the transfer equation reads:

$$\frac{d\mathcal{I}(\Omega, x)}{d\tau} = -\alpha\mathcal{I}(\Omega, x) + \alpha_{\text{abs}}B(x) + S(\Omega, x), \quad (8)$$

where  $\Omega$  denotes the photon propagation direction,  $x$  the spatial coordinate,  $\alpha$  and  $\alpha_{\text{abs}}$  the dimensionless extinction and absorption coefficient matrices respectively, and  $B$  the blackbody emission source term in the Stokes vector form [proportional to  $(1, 0, 0, 0)$  without polarization]. The differential extinction optical depth  $d\tau$  is related to the distance  $ds$  traveled along the propagation direction by  $d\tau = \lambda_{\text{ext}}^{-1}ds$ , where the reciprocal of extinction mean free path (MFP) is the sum of scattering and absorption components ( $\lambda_{\text{ext}}^{-1} = \lambda_{\text{abs}}^{-1} + \lambda_{\text{sca}}^{-1}$ ), which are related to the total cross sections via,

$$\lambda_{\text{abs}}^{-1} = \sum_i n_i \sigma_{\text{abs},i}, \quad \lambda_{\text{sca}}^{-1} = \sum_i n_i \sigma_{\text{sca},i}, \quad (9)$$

where  $n_i$  is the number density of the  $i$ th component that participates radiation-matter interactions, and  $\sigma_{\text{abs}}$  and  $\sigma_{\text{sca}}$  are the total cross sections of absorption and scattering, respectively. In practice, Kratos-polrad reads in both  $\lambda_{\text{abs}}^{-1}$  and  $\lambda_{\text{sca}}^{-1}$  spatial distribution profiles from input binary files, and the dimensionless  $\alpha$  and  $\alpha_{\text{abs}}$  matrices are calculated through every step of photon propagation. The scattering source term  $S$  describes how incident radiation from all directions is redistributed into direction  $\Omega$ ,

$$S(\Omega) = \oint d\Omega' Z(\Omega; \Omega') \mathcal{I}(\Omega'), \quad (10)$$

where  $Z(\Omega; \Omega')$  is the dimensionless scattering Mueller matrix. For anisotropic scattering by aligned dust grains or electrons,  $Z(\Omega; \Omega')$  depends on both the scattering angle and the local magnetic field orientation, requiring careful treatment of coordinate transformations.

Similar to established Monte Carlo radiative transfer codes (see e.g. [J. Steinacker et al. 2013](#) and references therein), Kratos-polrad numerically samples the polarized radiative transfer equations (eqs. 8 and 10) by propagating discrete photon packets through the computational domain, and locating the scattering events according to a scattering optical depth obeying exponential distribution generated stochastically at the moments when photons are generated or deflected by the previous scattering event. At each scattering event, the final direction and Stocks parameters are determined by sampling

the polarization-aware differential cross section, which is determined according to the properties of dust grains and photon wavelengths involved. The post-scattering photon properties, especially the Stokes parameters, are determined with the Mueller matrix in the coordinate frames of dust grains, where the coordinate transforms are conducted using the scheme described in §2.1. The differential cross section and Mueller matrix could be defined by the user prior to the execution of the program, either via analytical approximations, interpolation tables, or even artificial neural networks to be included in future works. Between scattering events, these packets traverse the simulation mesh from cell interface to cell interface, with each containing the necessary physical properties to model radiation-matter interactions ([L. Wang 2025b](#)).

The integration of photon packet extinction through each computational cell requires careful treatment, particularly in optically thick regimes where the assumption of linear absorption and emission becomes inadequate. In such cases, the cumulative effects of polarized extinction and emission along the propagation path exhibit non-linear behavior that cannot be accurately captured by simple linear approximations. To address this issue, Kratos-polrad implements analytical solutions to the polarized radiative transfer equations within individual cells, as detailed in Appendix A. The analytical treatment properly accounts for the coupled evolution of all four Stokes parameters, including the generation of circular polarization through differential phase delays and the transformation of polarization states through successive interactions. This approach ensures accurate evolution of the photon packets' Stokes parameters through regions of high optical depth, maintaining numerical stability and physical consistency even when traversing strongly absorbing and emitting media.

## 2.3. Efficient two-step imaging scheme

For direct comparisons with astronomical observations, synthetic polarimetry images are demanded. A naive imaging method based on Monte Carlo simulations would simply record photons that happen to exit the domain within the camera's solid angle. This approach, however, is proved to be computationally prohibitive because (1) the camera subtends an extremely small fraction of  $4\pi$  steradians, yielding minuscule photon counts; (2) multiple scattering events randomize photon directions, making direct imaging photons rare even in optically thick environments. Consequently, generating polarization maps without being limited by shot noise would require evolving prohibitive number of photon packets at a given viewing angle.



Kratos-polrad circumvents this inefficiency issue through a two-step approach that decouples scattering physics from imaging geometry. The method exploits the linearity of the radiative transfer equation and treats scattered photons as volumetric sources whose contribution to any viewing angle can be computed *a posteriori*. First, Kratos-polrad evolves photon packets through the domain using the standard Monte Carlo procedure, but with a modification: during propagation, each path integration segment (i.e., not only at scattering events) contributes to a scattering source function stored on the grid,

$$S(\Omega_{\text{cam}}, x) = \sum_{\text{pp}} S_{\text{pp}}(\Omega_{\text{cam}}, x). \quad (11)$$

Here  $\Omega_{\text{cam}}$  is fixed to the camera direction of interest, the subscript “pp” stands for “photon packet”, and  $\Omega_{\text{pp}}$  is the packet original propagation direction. Note that this accumulation occurs not just at discrete scattering events but continuously along the ray path, ensuring that single-scattering contributions are also captured. The summation runs through all photon packets, each carrying a Stokes vector  $\mathcal{I}_{\text{pp}}$ . In the discretized Monte Carlo scheme, the integral over solid angle becomes a summation over all photon packets traversing a computational cell, where the contribution of each photon packet follows  $S_{\text{pp}}(\Omega_{\text{cam}}, x) = Z(\Omega_{\text{cam}}; \Omega_{\text{pp}}) \mathcal{I}_{\text{pp}}$ . Note that this relation already includes the integration of incident directions of radiation, which is reduced because the angular distribution of the intensity of each photon packet is a Dirac delta function along its current propagation direction. Second, with  $S(\Omega_{\text{cam}}, x)$  properly sampled, Kratos-polrad perform a deterministic ray-tracing step by integrating eq. (8) along lines of sight toward the camera. When discretized, after traveling  $\delta l$  in each cell, the integration steps are performed using ray-marching algorithms that runs through the grid structures, with the same cell-by-cell analytic integration of the Stokes parameters described in §2.2 and Appendix A.

The second step in total significantly accelerates the imaging procedure, as the ray tracing is computationally much cheaper compared to the direct Monte Carlo imaging simulation whose most outgoing photons are discarded. On GPUs, Kratos-polrad implements this using a two-level parallelization scheme. At the top level, photon packets are distributed across streaming multi-processors (SMs), with each packet handled by a single GPU warp (or equivalently, “wavefronts” in some specific programming model). Within each warp, threads collaborate to accumulate contributions to  $S$  using shared memory reductions, minimizing global memory atomics (the scattering source function itself is stored in GPU global memory). When conducting imaging using this

architecture, Kratos-polrad could achieve a  $10^8$  photon sampling of the scattering source function within  $\sim 7$  seconds on a single RTX 5090 GPU (see also §3.1). The resulting speedup of  $\sim 10^2$  relative to traditional CPU-based polarized MCRT codes makes parameter-space exploration and high-resolution imaging synthesis feasible.

### 3. VERIFICATIONS

This section presents a comprehensive suite of tests and verifications to validate the proper implementation of the algorithms and methodologies described in §2. Through these validations, unless specifically noted, we adopt the dipole approximation for dust grain optical properties and rejection sampling of scattering differential cross sections (see also B. A. Whitney & M. J. Wolff 2002) for the simplicity and clarity of comparisons. More complicated dust grain models and stochastic sampling methods are, nonetheless, also possible in handling polarized radiative transfer in other realistic astrophysical scenarios. Together with the verification of physical accuracy, §3.1 also presents detailed performance benchmarks that quantify the computational efficiency of Kratos-polrad on modern GPU architectures. These benchmarks assess both strong and weak scaling behavior, compare performance across different hardware platforms, and evaluate the effectiveness and computational throughputs.

#### 3.1. Validation of Self-Scattering Polarization

We validate the treatment of self-scattering polarization through two complementary tests that probe different aspects of the radiative transfer implementation. The first test examines polarization generated purely by scattering in an inclined disk system. For photons initially emitted within a thin disk and scattered at oblique angles, the theoretical polarization fraction follows the analytical relation (H. Yang et al. 2016a):

$$p = \frac{\sin^2 i}{2 + \sin^2 i}, \quad (12)$$

where  $i$  denotes the disk inclination angle. This expression arises from the differential scattering cross-sections for polarized light and serves as a fundamental test of the scattering matrix implementation. Figure 1 compares our simulation results with this analytical prediction. The normalized Stokes parameter  $Q/I$  closely follows the theoretical curve across all inclination angles, while  $U/I$  remains consistent with zero (within numerical fluctuations), confirming the proper orientation of the polarization vectors relative to the scattering plane. Note that in Kratos-polrad, we always define a local Grain

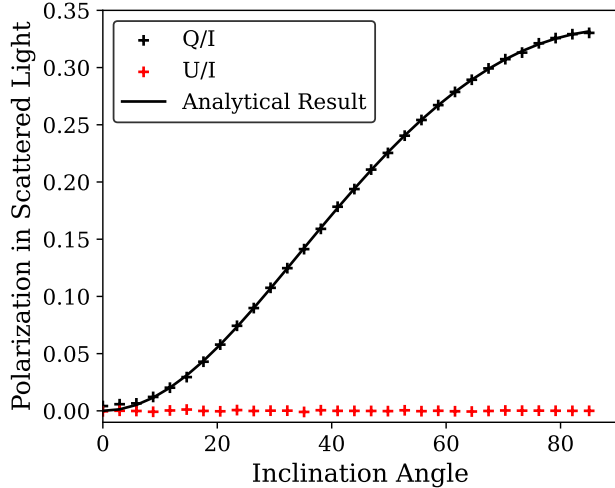


**Figure 1.** Validation of inclination-induced polarization in scattered light. Simulation results for  $Q/I$  (black markers) and  $U/I$  (red markers) are compared against the analytical solution (black curve). The agreement demonstrates correct implementation of scattering polarization dependencies.

Frame, which has its symmetric axis along  $x$ -direction in this test, even though the dust grains are in isotropic Rayleigh scattering regime. The good agreement confirms that Kratos-polrad can handle isotropic spherical dust grains very well.

The second test addresses the critical balance between scattered radiation and direct thermal emission during imaging synthesis. This balance is non-trivial as it requires proper treatment of both source terms during ray tracing. For spherical dust grains, direct thermal emission dilutes polarization signals, while for aligned irregular grains, the interplay becomes more complex due to additional polarization from emission. We configured a cylindrical dust distribution with isothermal temperature  $T = 30$  K and Gaussian density profile  $\rho(r) = \rho_0 \exp[-(r/r_0)^2]$ , similar to the test in (A. Kataoka et al. 2015). The dust composition follows astronomical silicate (B. T. Draine 2003) with an MRN size distribution (J. S. Mathis et al. 1977) and maximum grain size  $a_{\max} = 14 \mu\text{m}$ , ensuring validity of the dipole approximation currently implemented in Kratos-polrad. Figure 2 presents polarized intensity maps with overlaid polarization vectors. The right panel compares polarization fractions (defined as  $Q/I$ ) along the  $x = 0$  cut between Kratos-polrad and RADMC-3D. The excellent agreement in polarization fraction validates our implementation, while differences near boundaries arise from our use of periodic boundary conditions, which eliminate edge artifacts towards  $x$ -boundaries present in the

RADMC-3D simulation, as well as reducing the parallel polarization towards  $y$ -boundaries.

Based on the same test problem, we benchmarked computational performance against RADMC-3D, with results shown in Figure 3. The GPU-accelerated Kratos-polrad demonstrates superior scaling, with computation time growing approximately linearly with photon number. On both NVIDIA (RTX series) and AMD (7900XTX) hardware, Kratos-polrad exceeds CPU performance by over an order of magnitude. Notably, Kratos-polrad maintains this performance advantage while including polarized absorption processes that RADMC-3D simplifies. The RTX 3090 achieves throughput equivalent to  $\sim 80$  CPU cores of AMD Ryzen 7950X, while the RTX 5090 matches  $\sim 320$  CPU cores, highlighting the transformative potential of GPU acceleration for polarized radiative transfer calculations.

### 3.2. Polarization Rotation in Twisted Magnetic Fields

To validate the accurate treatment of polarization state transformations during propagation through magnetically aligned media, we designed a test scenario involving light propagation through a slab with spatially varying magnetic field orientations. This test specifically examines the rotation behavior of Stokes parameters as photons traverse regions with continuously changing grain alignment directions. We constructed a simulation domain consisting of a slab with total optical depth  $\tau_{\text{total}} = 1$  embedded with a twisting magnetic field configuration. The magnetic field vector varies sinusoidally throughout the slab with zero  $z$ -component and spatially varying  $x$ - and  $y$ -components:

$$B_x(\tau) = B_0 \cos(2\pi\tau), \quad B_y(\tau) = B_0 \sin(2\pi\tau), \quad (13)$$

where  $\tau$  represents the optical depth coordinate through the slab. This configuration creates a magnetic field that rotates continuously by  $360^\circ$  across the slab thickness, as illustrated in the top panel of Figure 4.

We initialized  $10^3$  unpolarized photons distributed randomly throughout the slab volume. These photons propagate vertically through the medium until exiting the simulation domain. During propagation, they experience dichroic extinction due to dust grains aligned with the local magnetic field direction, with each interaction inducing polarization dependent on the grain orientation relative to the photon's propagation direction and polarization state.

In the optically thin limit, where polarization from secondary extinction can be neglected, the emergent polarization can be derived analytically by integrating the contributions from successive layers with varying magnetic field orientations, each operating on their own non-

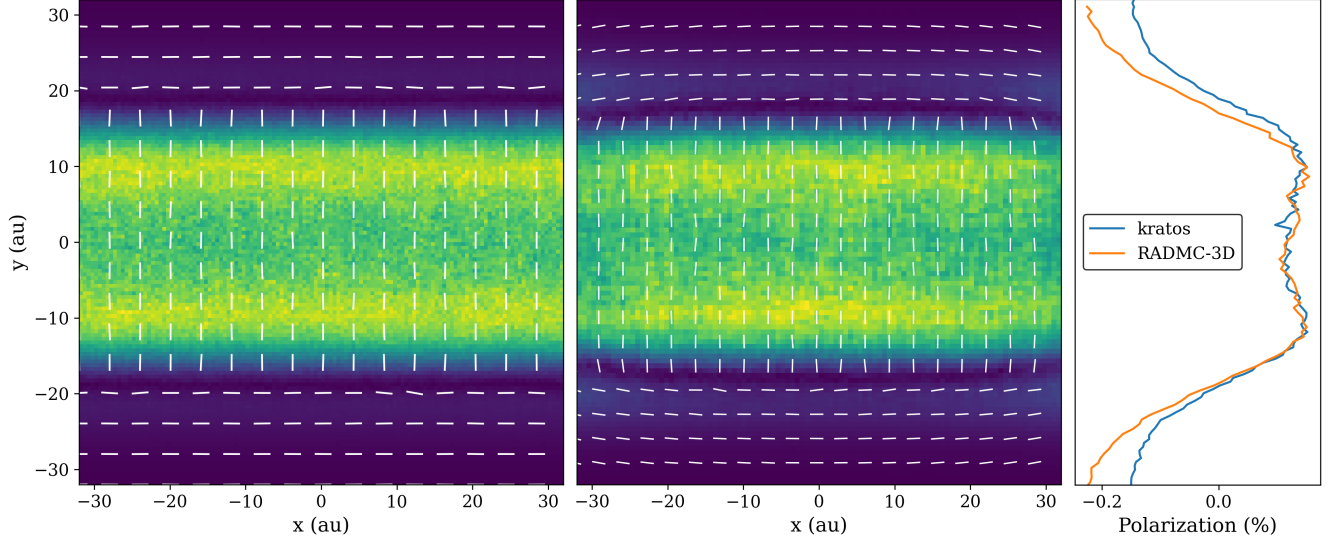


**Figure 2.** Comparison of self-scattering polarization in a dust cylinder. **Left:** Kratos-polrad simulation showing polarized intensity (heatmap) and orientation (line segments). **Middle:** Equivalent RADMC-3D results. **Right:** Polarization fraction profiles along  $x = 0$  demonstrate code agreement, with boundary differences attributable to periodic conditions in Kratos-polrad.

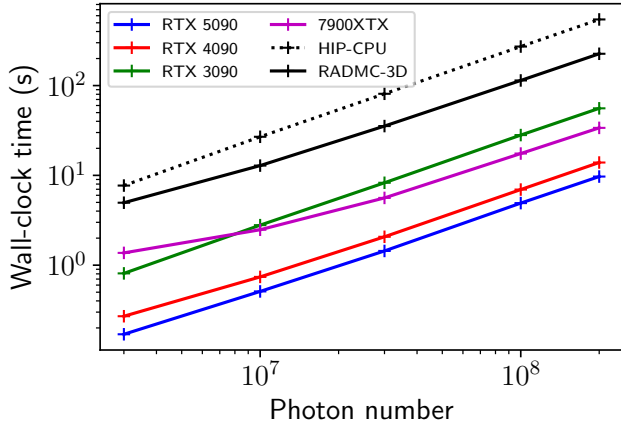


**Figure 3.** Speed test using the same physical layout described in §3.1, showing the performance of Kratos-polrad with varying numbers of simulated photon packets compared to RADMC-3D. The HIP-CPU case conducts Kratos-polrad calculations using the AMD Ryzen 7950X CPU, which is the same device used by the RADMC-3D tests. Other tests using RTX devices and 7900XTX are conducted on GPUs.

polarized photons. For initially unpolarized light passing through the twisting field configuration, the analytical expressions for the normalized Stokes parameters are,

$$\begin{cases} \frac{Q}{I} = \frac{p_0}{4\pi} \sin(4\pi\tau) \\ \frac{U}{I} = -\frac{p_0}{4\pi} [1 - \cos(4\pi\tau)] \\ \frac{V}{I} = \left(\frac{p_0}{4\pi}\right)^2 [\sin(4\pi\tau) - 4\pi\tau] \end{cases}, \quad (14)$$

where  $p_0$  represents the intrinsic polarization fraction in the optically thin limit, determined by the dielectric function and aspect ratio of the dust grains.

The extinction matrix, calculated using the dipole approximation and optical theorem, contains no phase lag between differently polarized dipole excitations. Consequently, there are no direct cross-terms between Stokes  $U$  and  $V$  in the physical extinction process. To test the code's handling of potential cross-terms, we artificially introduced a  $U$ - $V$  coupling term identical to the  $I$ - $Q$  cross-term in the extinction matrix. This modification enables the generation of appreciable circular polarization from initially unpolarized light through the twisting field configuration, even in the dipole approximation regime, providing a stringent test of the coordinate transformation implementation.

Figure 4 presents the comparison between simulation results and analytical predictions. The emergent polarization states of photons, plotted as functions of their generation optical depth  $\tau$ , show excellent agreement with the analytical solutions. The simulation data (red dots) closely follow the theoretical curves (blue lines) for all Stokes parameters. The residual differences, magnified by a factor of 50 and shown as green dots, reveal two distinct patterns: small-scale fluctuations attributable to numerical errors within individual grid cells, and larger-scale variations arising from the optical thin approximation used in deriving the analytical solutions. Despite these minor discrepancies, the overall agreement demonstrates the correctness of the quaternion-based

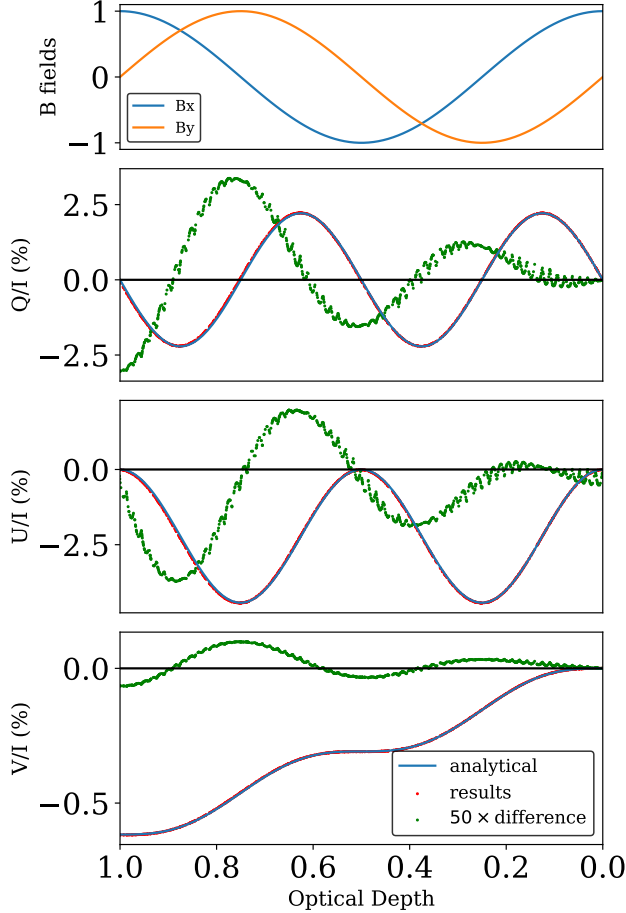


**Figure 4.** Emergent polarization from a slab with twisting magnetic fields. **Top panel:** Magnetic field configuration showing continuous rotation across the slab. **Lower panels:** Normalized Stokes parameters  $Q/I$ ,  $U/I$ , and  $V/I$  as functions of generation optical depth. Simulation results (red dots) show excellent agreement with analytical predictions (blue lines). Residual differences (green dots, magnified 50 $\times$ ) demonstrate the accuracy of the polarization transformation implementation.

coordinate transformation implementation in handling the complex polarization state rotations through media with spatially varying alignment directions.

### 3.3. Validation of Dichroic Extinction by Aligned Grains

The accurate treatment of dichroic thermal emission and extinction by aligned, non-spherical dust grains represents a fundamental capability for simulating polarized radiation in magnetized environments. To validate this critical component, we examine the polarization behavior arising from pure dichroic extinction in a uniformly aligned dust slab without scattering contributions. The theoretical polarization fraction for such a

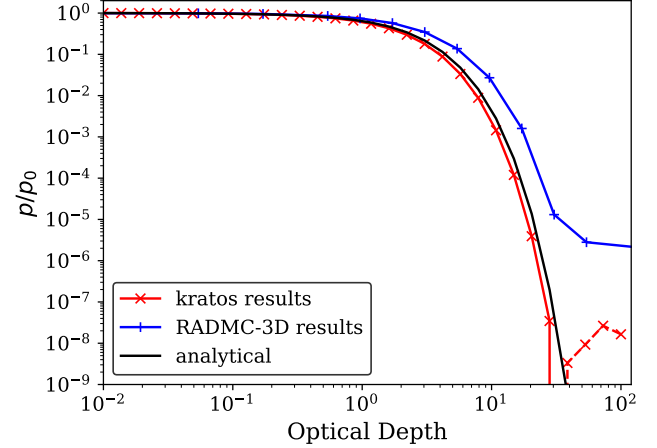


**Figure 5.** Polarization fraction as a function of optical depth in a uniformly aligned dust slab. Simulation results from Kratos-polrad (red) show excellent agreement with analytical theory (black) up to  $\tau \approx 30$ , outperforming RADMC-3D (blue) in the high-optical-depth regime. The polarization is reversed at high optical depth in Kratos-polrad results, shown as dashed lines.

system follows the analytical expression derived by [R. H. Hildebrand et al. \(2000\)](#):

$$P = \frac{e^{-\tau} \sinh(p_0 \tau)}{1 - e^{-\tau} \cosh(p_0 \tau)}, \quad (15)$$

where  $\tau$  denotes the optical depth and  $p_0$  represents the intrinsic polarization determined by grain aspect ratio, dielectric properties, and viewing angle relative to the grain alignment axis.

Figure 5 compares our simulation results (red curves) with this analytical solution (black curve). The Kratos-polrad implementation demonstrates excellent agreement with theory up to  $\tau \approx 30$ , beyond which numerical truncation errors become significant as polarization signals approach the noise floor. We further compare our results with RADMC-3D, which also implements dichroic processes. As shown by the blue curve in Figure 5, RADMC-3D begins to deviate from the theoretical solution at  $\tau \sim 3$ , earlier than Kratos-polrad. This improved performance stems from our implementation of analytical solutions to the extinction matrix within each computational cell, enhancing numerical stability in optically thick regimes. Nevertheless, these differences remain negligible for practical applications since the polarization fraction from dichroic processes is usually below observational limits at this high optical depth.

### 3.4. Scattering by Grains in Plane-parallel Atmospheres

To validate polarized scattering in more complex environments, we simulate radiation transfer through



a plane-parallel atmosphere containing aligned dust grains, following the methodology of Z.-Y. D. Lin et al. (2022). The uniform slab incorporates dust grains with aspect ratio  $s = 1.03$  and magnetic field alignment along the x-axis, creating conditions where scattering and emission processes interact significantly at moderate optical depths. We fix the line-of-sight inclination at  $45^\circ$  while varying the azimuthal viewing angle to probe the full polarization response.

Figure 6 presents the resulting Stokes parameters  $Q/I$  and  $U/I$  as functions of viewing angle for different optical depths. The polarization patterns reveal two distinct components: a modulated contribution from direct thermal emission that varies with viewing geometry relative to grain orientation, and a scattering-induced component that produces a non-zero offset in Stokes  $Q$ . The emission modulation diminishes with increasing optical depth, consistent with the damping behavior described by Equation 15. The Stokes parameter  $U$  oscillates around zero as expected for this symmetric configuration, while Stokes  $Q$  exhibits a characteristic offset from self-scattering polarization. This offset displays non-monotonic dependence on optical depth, initially increasing until  $\tau \sim 1$  before declining to an asymptotic value of approximately 1%, in agreement with the findings of H. Yang et al. (2017). These results demonstrate excellent consistency with established benchmarks, validating our implementation of polarized scattering by aligned grains.

### 3.5. Scattering of Central Starlight by Aligned Grains

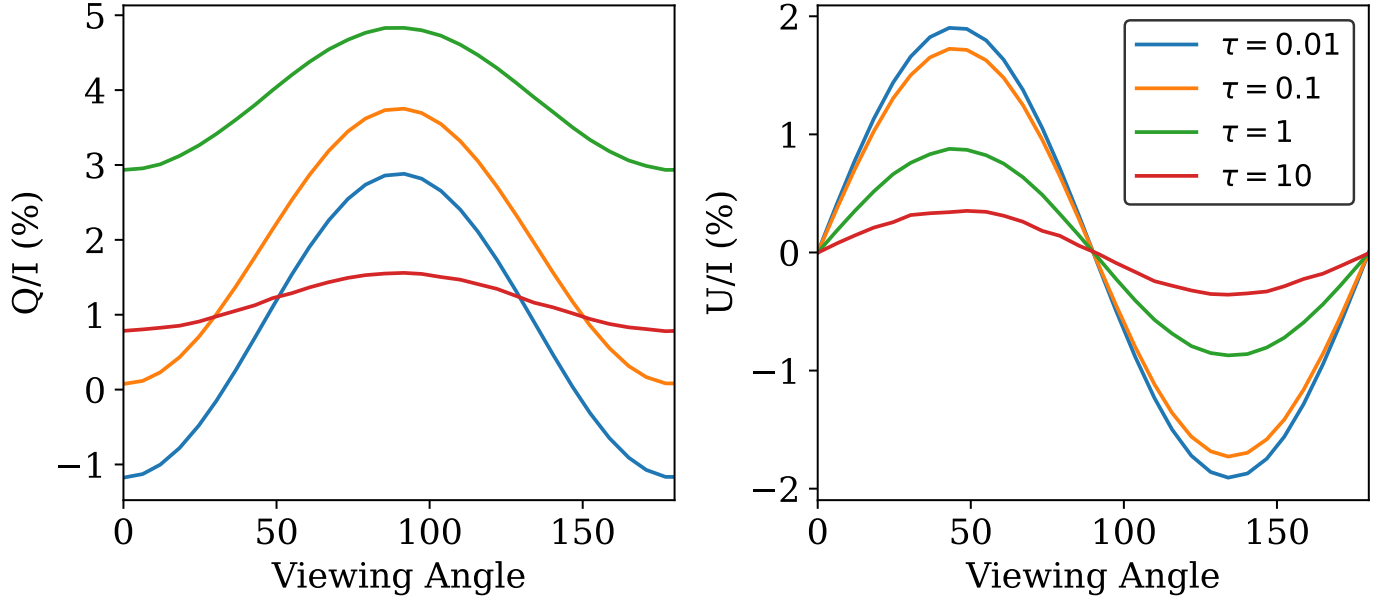
To validate our implementation against established benchmarks, we reproduce the test case introduced by B. A. Whitney & M. J. Wolff (2002) in their HOCHUNK radiative transfer code. This test examines polarized scattering by magnetically aligned, irregular dust grains in a circumstellar environment, using a uniform spherical distribution as a computationally tractable yet physically relevant configuration. We configure a uniform sphere of radius 20 au with a homogeneous magnetic field oriented along the z-axis. Dust grains are modeled as perfect oblate spheroids with short axes aligned parallel to the magnetic field direction. For the grain properties, we adopt a complex refractive index  $m = 2.30 + 0.0228i$  and aspect ratio 2:1, similar to the implementation of (B. A. Whitney & M. J. Wolff 2002).

Figure 7 presents the resulting polarization patterns for three characteristic optical depths ( $\tau = 0.01, 1$ , and 10), viewed along the x-axis perpendicular to the magnetic field direction. In the optically thin regime ( $\tau = 0.01$ ), the polarization pattern exhibits, to the leading order, concentric modulation reflecting the central

illuminating source. Grains aligned with their long axes horizontally produce preferential scattering that reduces polarization along this direction, creating a distinctive figure-8 morphology in the polarization map. As optical depth increases to  $\tau = 1$ , this pattern expands while maintaining its fundamental character, demonstrating the growing influence of scattering. The optically thick case ( $\tau = 10$ ) reveals a qualitatively different pattern dominated by dichroic extinction. Foreground grains preferentially absorb radiation polarized along their long axes, resulting in polarization aligned with the magnetic field direction in the central regions. This transition from scattering-dominated to extinction-dominated polarization represents a critical validation of our code's ability to handle the complex interplay between different polarization mechanisms across optical depth regimes. Circular polarization patterns remain qualitatively consistent across optical depths, with lower polarization fractions in central regions compared to outer areas. However, our implementation produces systematically lower circular polarization fractions than B. A. Whitney & M. J. Wolff (2002), which we attribute to differences in the treatment of grain optics. Our dipole approximation assumes minimal phase lag between dipole excitations along different grain axes, relying primarily on the imaginary component of the dielectric function to generate Stokes  $I$ - $V$  coupling. The predominantly refractory nature of our dust model ( $\text{Im}[m] \ll \text{Re}[m]$ ) further suppresses circular polarization generation compared to more absorptive grain compositions.

## 4. SUMMARY

This paper has presented the development, verification, and performance characterization of Kratos-polrad, a novel GPU-accelerated Monte Carlo radiative transfer code specifically designed for polarization calculations in astrophysical environments. The core features of Kratos-polrad include a comprehensive treatment of full Stokes parameters throughout photon propagation and scattering events. Based on efficient coordinate transformations using quaternion algebra, complex polarization state rotations in magnetically aligned media is accomplished with ease. The two-step imaging approach that decouples Monte Carlo sampling of scattering source functions from viewing geometry significantly enhance the efficiency of polarimetry imaging. Through extensive validation against analytical solutions and established codes, we have demonstrated the code accuracy in handling diverse polarization phenomena, including dichroic extinction in aligned dust grains, self-scattering polarization in inclined disks, and complex polarization patterns in twisted magnetic field



**Figure 6.** Polarization patterns in plane-parallel atmospheres with aligned dust grains. Stokes parameters  $Q/I$  and  $U/I$  are shown as functions of azimuthal viewing angle at fixed  $45^\circ$  inclination for different optical depths. Results demonstrate the interplay between direct emission modulation and scattering-induced polarization, showing excellent agreement with established benchmarks.

configurations. Kratos-polrad achieves performance improvements of  $\sim 10^2$  times compared to traditional CPU-based methods, while maintaining physical accuracy across diverse test scenarios.

The computational performance of Kratos-polrad enables previously prohibitive studies in polarimetric astrophysics. The ability to generate high-signal-to-noise polarization maps from  $10^8$  photon packets within  $\sim 10^1$  seconds (or even faster) on consumer-grade GPUs opens new possibilities for parameter-space explorations and high-resolution imaging of complex astrophysical systems. When necessary, the modular architecture of Kratos could also facilitate coupling with hydrodynamic simulations from the base Kratos framework, paving the way for time-dependent simulations preparing for prospective transient observations studying the polarimetric observables in multiple astrophysical scenarios including protoplanetary disks and exoplanetary atmospheres.

Looking forward, several promising directions emerge for extending the capabilities of Kratos-polrad. A particularly compelling avenue involves the integration of deep neural networks for handling the complex optical properties of realistic dust grain populations. Contemporary dust models must account for distributions in

grain sizes, shapes (including fractal dimensions and filling factors), compositions, and alignment properties, resulting in multi-dimensional functions mapping the incident photon configurations (direction and Stokes parameters) to the scattered photon properties. High-dimensional interpolation tables, however, typically consume significant memory and computational resources beyond the capacity of efficient Monte Carlo simulations. We thus expect implementing neural network-based emulators, which can learn the mapping from grain parameters to Mueller matrix elements, to facilitate efficient evaluation of scattering properties without expensive table lookups or prohibitive on-the-fly calculations. Such an approach would dramatically reduce memory requirements while maintaining accuracy through carefully designed network architectures and training procedures, extending the capabilities of exploring more complicated but realistic systems involved in the observational studies in dusty astrophysical systems.

#### ACKNOWLEDGMENTS

This work is supported by the National Natural Science Foundation of China (NSFC) [12473067].

#### REFERENCES

- Andersson, B.-G., Lazarian, A., & Vaillancourt, J. E. 2015, *ARA&A*, 53, 501, doi: [10.1146/annurev-astro-082214-122414](https://doi.org/10.1146/annurev-astro-082214-122414)
- Benisty, M., Dominik, C., Follette, K., et al. 2023, in *Astronomical Society of the Pacific Conference Series*, Vol. 534, *Protostars and Planets VII*, ed. S. Inutsuka, Y. Aikawa, T. Muto, K. Tomida, & M. Tamura, 605, doi: [10.48550/arXiv.2203.09991](https://doi.org/10.48550/arXiv.2203.09991)

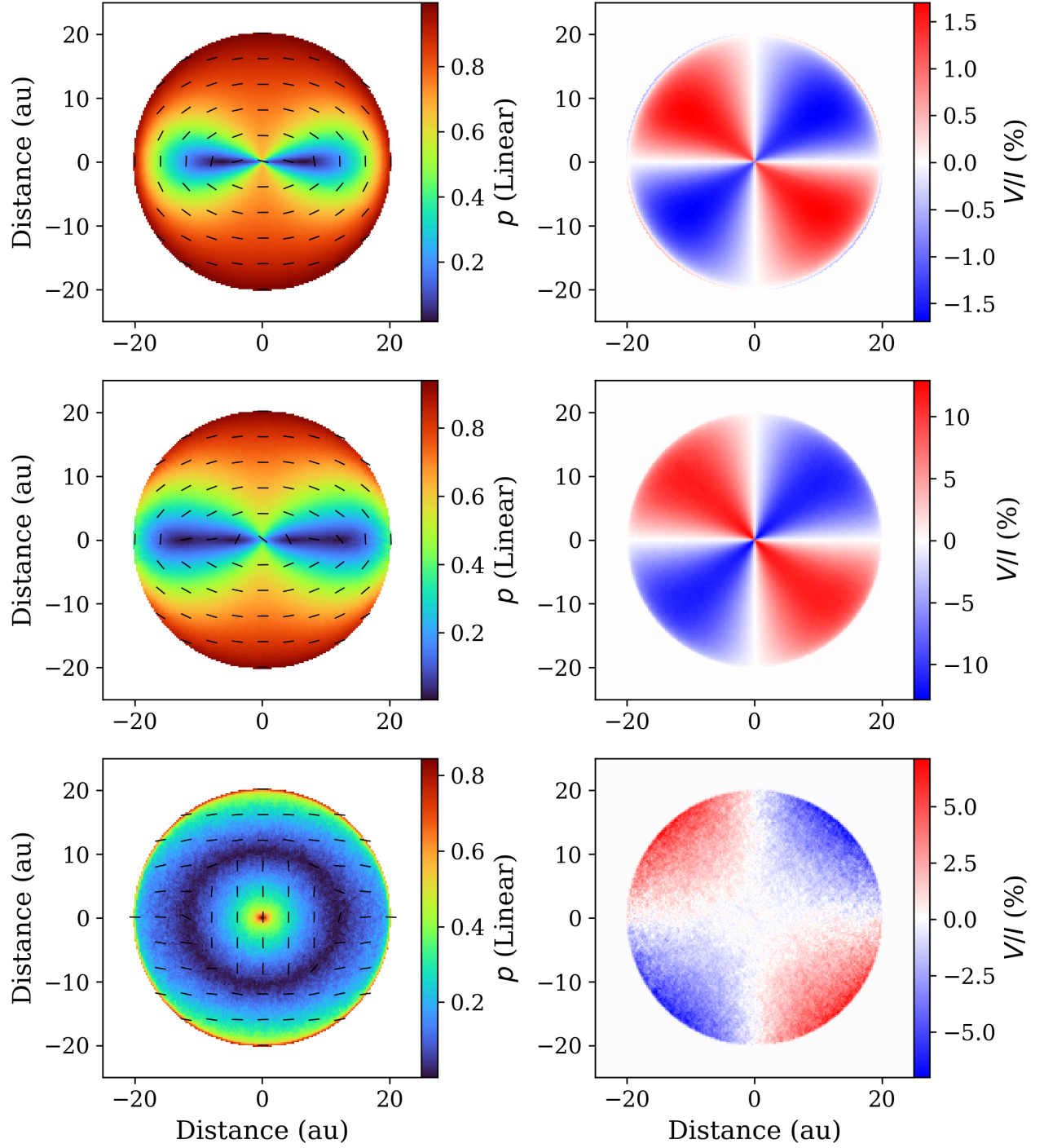


**Figure 7.** Polarization patterns from scattering by aligned dust grains in a uniform sphere. **Top to bottom:** Results for optical depths  $\tau = 0.01, 1$ , and  $10$ . **Left column:** Linear polarization fraction with overlaid orientation vectors. **Right column:** Circular polarization fraction. The transition from scattering-dominated to extinction-dominated regimes is clearly visible with increasing optical depth.

- Bocchio, M., Marassi, S., Schneider, R., et al. 2016, *A&A*, 587, A157, doi: [10.1051/0004-6361/201527432](https://doi.org/10.1051/0004-6361/201527432)
- Boyle, M., Bonnett, B., Long, J., et al. 2025,, v2024.0.12 Zenodo, doi: [10.5281/zenodo.17082991](https://doi.org/10.5281/zenodo.17082991)
- Byrohl, C., & Nelson, D. 2025, arXiv e-prints, arXiv:2507.11603, doi: [10.48550/arXiv.2507.11603](https://doi.org/10.48550/arXiv.2507.11603)
- Camps, P., & Baes, M. 2015, *Astronomy and Computing*, 9, 20, doi: [10.1016/j.ascom.2014.10.004](https://doi.org/10.1016/j.ascom.2014.10.004)
- Camps, P., & Baes, M. 2020, *Astronomy and Computing*, 31, 100381, doi: [10.1016/j.ascom.2020.100381](https://doi.org/10.1016/j.ascom.2020.100381)
- Chandrasekhar, S. 1960, *Radiative transfer*
- Cooray, A., Meixner, M., Leisawitz, D., et al. 2019, in *Bulletin of the American Astronomical Society*, Vol. 51, 59
- Draine, B. T. 2003, *ApJ*, 598, 1017, doi: [10.1086/379118](https://doi.org/10.1086/379118)
- Dullemond, C. P., Juhasz, A., Pohl, A., et al. 2012,, *Astrophysics Source Code Library*, record ascl:1202.015 <http://ascl.net/1202.015>
- Hall, J. S. 1949, *Science*, 109, 166, doi: [10.1126/science.109.2825.166](https://doi.org/10.1126/science.109.2825.166)
- Hildebrand, R. H., Davidson, J. A., Dotson, J. L., et al. 2000, *PASP*, 112, 1215, doi: [10.1086/316613](https://doi.org/10.1086/316613)
- Hiltner, W. A. 1949, *Science*, 109, 165, doi: [10.1126/science.109.2825.165](https://doi.org/10.1126/science.109.2825.165)
- Kartje, J. F. 1995, *ApJ*, 452, 565, doi: [10.1086/176329](https://doi.org/10.1086/176329)
- Kataoka, A., Muto, T., Momose, M., et al. 2015, *ApJ*, 809, 78, doi: [10.1088/0004-637X/809/1/78](https://doi.org/10.1088/0004-637X/809/1/78)
- Lazarian, A., & Hoang, T. 2007, *MNRAS*, 378, 910, doi: [10.1111/j.1365-2966.2007.11817.x](https://doi.org/10.1111/j.1365-2966.2007.11817.x)
- Lin, Z.-Y. D., Li, Z.-Y., Yang, H., et al. 2024a, *MNRAS*, 534, 3713, doi: [10.1093/mnras/stae2248](https://doi.org/10.1093/mnras/stae2248)
- Lin, Z.-Y. D., Li, Z.-Y., Yang, H., et al. 2022, *MNRAS*, 512, 3922, doi: [10.1093/mnras/stac753](https://doi.org/10.1093/mnras/stac753)
- Lin, Z.-Y. D., Li, Z.-Y., Stephens, I. W., et al. 2024b, *MNRAS*, 528, 843, doi: [10.1093/mnras/stae040](https://doi.org/10.1093/mnras/stae040)
- Malik, M., Grosheintz, L., Mendonça, J. M., et al. 2017, *AJ*, 153, 56, doi: [10.3847/1538-3881/153/2/56](https://doi.org/10.3847/1538-3881/153/2/56)
- Marin, F., Goosmann, R. W., & Gaskell, C. M. 2015, *A&A*, 577, A66, doi: [10.1051/0004-6361/201525628](https://doi.org/10.1051/0004-6361/201525628)
- Mathis, J. S., Rumpl, W., & Nordsieck, K. H. 1977, *ApJ*, 217, 425, doi: [10.1086/155591](https://doi.org/10.1086/155591)
- Pinte, C., Ménard, F., Duchêne, G., & Bastien, P. 2006, *A&A*, 459, 797, doi: [10.1051/0004-6361:20053275](https://doi.org/10.1051/0004-6361:20053275)
- Ramstedt, S., Maercker, M., Olofsson, G., Olofsson, H., & Schöier, F. L. 2011, *A&A*, 531, A148, doi: [10.1051/0004-6361/201015964](https://doi.org/10.1051/0004-6361/201015964)
- Reissl, S., Wolf, S., & Brauer, R. 2016, *A&A*, 593, A87, doi: [10.1051/0004-6361/201424930](https://doi.org/10.1051/0004-6361/201424930)
- Robitaille, T. P. 2011, *A&A*, 536, A79, doi: [10.1051/0004-6361/201117150](https://doi.org/10.1051/0004-6361/201117150)
- Schmid, H. M., Bazzon, A., Roelfsema, R., et al. 2018, *A&A*, 619, A9, doi: [10.1051/0004-6361/201833620](https://doi.org/10.1051/0004-6361/201833620)
- Seager, S., Whitney, B. A., & Sasselov, D. D. 2000, *ApJ*, 540, 504, doi: [10.1086/309292](https://doi.org/10.1086/309292)
- Steinacker, J., Baes, M., & Gordon, K. D. 2013, *ARA&A*, 51, 63, doi: [10.1146/annurev-astro-082812-141042](https://doi.org/10.1146/annurev-astro-082812-141042)
- Stephens, I. W., Lin, Z.-Y. D., Fernández-López, M., et al. 2023, *Nature*, 623, 705, doi: [10.1038/s41586-023-06648-7](https://doi.org/10.1038/s41586-023-06648-7)
- Stolker, T., Min, M., Stam, D. M., et al. 2017, *A&A*, 607, A42, doi: [10.1051/0004-6361/201730780](https://doi.org/10.1051/0004-6361/201730780)
- Tazaki, R., Lazarian, A., & Nomura, H. 2017, *ApJ*, 839, 56, doi: [10.3847/1538-4357/839/1/56](https://doi.org/10.3847/1538-4357/839/1/56)
- Wang, L. 2025a, *ApJS*, 277, 63, doi: [10.3847/1538-4365/adbdb6](https://doi.org/10.3847/1538-4365/adbdb6)
- Wang, L. 2025b, arXiv e-prints, arXiv:2504.04941, doi: [10.48550/arXiv.2504.04941](https://doi.org/10.48550/arXiv.2504.04941)
- Whitney, B. A., Robitaille, T. P., Bjorkman, J. E., et al. 2013, *ApJS*, 207, 30, doi: [10.1088/0067-0049/207/2/30](https://doi.org/10.1088/0067-0049/207/2/30)
- Whitney, B. A., & Wolff, M. J. 2002, *ApJ*, 574, 205, doi: [10.1086/340901](https://doi.org/10.1086/340901)
- Yang, H., & Li, Z.-Y. 2022, *AJ*, 164, 99, doi: [10.3847/1538-3881/ac7ffc](https://doi.org/10.3847/1538-3881/ac7ffc)
- Yang, H., Li, Z.-Y., Looney, L., & Stephens, I. 2016a, *MNRAS*, 456, 2794, doi: [10.1093/mnras/stv2633](https://doi.org/10.1093/mnras/stv2633)
- Yang, H., Li, Z.-Y., Looney, L. W., et al. 2016b, *MNRAS*, 460, 4109, doi: [10.1093/mnras/stw1253](https://doi.org/10.1093/mnras/stw1253)
- Yang, H., Li, Z.-Y., Looney, L. W., Girart, J. M., & Stephens, I. W. 2017, *MNRAS*, 472, 373, doi: [10.1093/mnras/stx1951](https://doi.org/10.1093/mnras/stx1951)
- Yang, H., Li, Z.-Y., Stephens, I. W., Kataoka, A., & Looney, L. 2019, *MNRAS*, 483, 2371, doi: [10.1093/mnras/sty3263](https://doi.org/10.1093/mnras/sty3263)

## APPENDIX

## A. SOLUTION TO RADIATIVE TRANSFER

Once the vector source function per extinction optical depth ( $S_1, S_2, S_3, S_4$ ) (including the emission source function, and the scattering source function if applied in the imaging step; see also §2.2) has been determined, we recast the radiative transfer equation (eq. 8) in the following expanded form,

$$\frac{d}{d\tau} \begin{bmatrix} I \\ Q \\ U \\ V \end{bmatrix} = - \begin{bmatrix} \alpha_1 & \alpha_2 & 0 & 0 \\ -\alpha_2 & \alpha_1 & 0 & 0 \\ 0 & 0 & \alpha_1 & \alpha_3 \\ 0 & 0 & \alpha_3 & \alpha_1 \end{bmatrix} \begin{bmatrix} I \\ Q \\ U \\ V \end{bmatrix} + \begin{bmatrix} S_1 \\ S_2 \\ S_3 \\ S_4 \end{bmatrix}, \quad (\text{A1})$$

where  $d\tau$  denotes the differential extinction optical depth (combining absorption and scattering) along the propagation path of a photon packet. The matrix elements  $\alpha_i$  ( $i = 1, 2, 3$ ) are determined based on dust grain properties (in case of dipole grain approximation, for example, see also the appendix of [H. Yang & Z.-Y. Li 2022](#)). Let  $(I_0, Q_0, U_0, V_0)$  be the Stokes parameters entering this cell, and  $d\tau$  be the extinction optical depth of the light trans-passing this cell. With extinction optical depth  $\delta\tau$  (which could be optically thick) measured in one cell from one cell interface to another, the Stokes parameters of the light after propagating through the cell can be solved analytically,

$$\begin{aligned} I &= I_s + (I_0 - I_s)e^{-\alpha_1\delta\tau} \cosh(-\alpha_2\delta\tau) \\ &\quad + (Q_0 - Q_s)e^{-\alpha_1\delta\tau} \sinh(-\alpha_2\delta\tau), \\ Q &= Q_s + (I_0 - I_s)e^{-\alpha_1\delta\tau} \sinh(-\alpha_2\delta\tau) \\ &\quad + (Q_0 - Q_s)e^{-\alpha_1\delta\tau} \cosh(-\alpha_2\delta\tau), \\ U &= U_s + (U_0 - U_s)e^{-\alpha_1\delta\tau} \cos(-\alpha_3\delta\tau) \\ &\quad + (V_0 - V_s)e^{-\alpha_1\delta\tau} \sin(-\alpha_3\delta\tau), \\ V &= V_s - (U_0 - U_s)e^{-\alpha_1\delta\tau} \sin(-\alpha_3\delta\tau) \\ &\quad + (V_0 - V_s)e^{-\alpha_1\delta\tau} \cos(-\alpha_3\delta\tau), \end{aligned} \quad (\text{A2})$$

where the auxiliary quantities are defined as,

$$\begin{aligned} I_s &= \frac{\alpha_1 S_1 - \alpha_2 S_2}{\alpha_1^2 - \alpha_2^2} \\ Q_s &= \frac{\alpha_1 S_2 - \alpha_2 S_1}{\alpha_1^2 - \alpha_2^2} \\ U_s &= \frac{\alpha_1 S_3 - \alpha_3 S_4}{\alpha_1^2 + \alpha_3^2} \\ V_s &= \frac{\alpha_1 S_4 + \alpha_3 S_3}{\alpha_1^2 + \alpha_3^2} \end{aligned} \quad (\text{A3})$$